Eur. Phys. J. B **53**, 91–98 (2006)
DOI: 10.1140/epjb/e2006-00346-y

THE EUROPEAN PHYSICAL JOURNAL B

Phonon-induced decoherence and dissipation in donor-based charge qubits

J. Eckel[a], S. Weiss, and M. Thorwart

Institut für Theoretische Physik IV, Heinrich-Heine-Universität Düsseldorf, 40225 Düsseldorf, Germany

Received 24 May 2006 / Received in final form 20 July 2006
Published online 7 September 2006 –

Abstract. We investigate the phonon-induced decoherence and dissipation in a donor-based charge quantum bit realized by the orbital states of an electron shared by two dopant ions which are implanted in a silicon host crystal. The dopant ions are taken from the group-V elements Bi, As, P, Sb. The excess electron is coupled to deformation potential acoustic phonons which dominate in the Si host. The particular geometry tailors a non-monotonous frequency distribution of the phonon modes. We determine the exact qubit dynamics under the influence of the phonons by employing the numerically exact quasi-adiabatic propagator path integral scheme thereby taking into account all bath-induced correlations. In particular, we have improved the scheme by completely eliminating the Trotter discretization error by a Hirsch-Fye extrapolation. By comparing the exact results to those of a Born-Markov approximation we find that the latter yields appropriate estimates for the decoherence and relaxation rates. However, noticeable quantitative corrections due to non-Markovian contributions appear.

PACS. 03.67.Lx Quantum computation – 63.20.Kr Phonon-electron and phonon-phonon interactions – 03.65.Yz Decoherence; open systems; quantum statistical methods

1 Introduction

During the last decade it turned out that solid-state based nano structures are promising candidates for the realization of quantum information processing devices [1]. The building blocks are quantum mechanical two-state systems (qubits) and some of the proposed designs have been realized in groundbreaking experiments, see reference [1] for a recent review on this field. Thereby, various approaches have been undertaken, ranging from superconducting flux and charge qubit devices to devices using the spin or the charge degrees of freedom of individual electrons in confined geometries. Aiming at an extreme miniaturization of solid-state devices down to the nm-scale, it has been proposed to implant individual dopant atoms in a semiconductor crystal and to use nuclear spin states of buried phosphorus dopants to realize a spin-qubit (Kane's proposal [2]). Complementary to the Kane architecture, the charge degree of freedom of a single electron shared by two donor atoms in a host crystal can be used for the coding of the logical information, as proposed in references [3,4]. Thereby, the logical states $|0\rangle$ and $|1\rangle$ are realized by the charge states of the double-donor-system with the excess electron either located on the left or on the right donor. The transition between these states occurs via tunneling of the electron between the two dopants. The charge qubits can in principle be controlled efficiently by external electric fields, e.g., by an applied gate voltage. This property renders the proposed architecture attractive for realizing control schemes with available fabrication and read-out technologies [4]. Experimental progress for this kind of ion-implanted Si:P nanostructures has been reported recently [5].

On the other hand, solid-state qubits suffer from the large number of degrees of freedom due to their embedding in a complex many-particle environment. The environmental decoherence and dissipation lead to a deterioration of the performance of quantum logic operations and also strongly influence entanglement between qubits [6] necessary for quantum gate operations. Various sources of decoherence include nuclear spins, phonons, and electromagnetic fluctuations in the host crystal. To gain a detailed understanding of the various decoherence mechanisms, realistic model calculations have to be performed which then allow to sort out the different contributions. In this work we concentrate on the influence of a phonon bath on the shared electron. To be definite, we consider a charge qubit formed by two group-V donors as proposed in reference [7]. One donor is formed by a phosphorus atom while the second donor will be one of the class {Bi, As, P, Sb}. The donor pair is assumed to be implanted in a silicon crystal host and share a common electron. We consider linear acoustic phonons coupled to the electron and determine the dynamics of the charge

[a] e-mail: eckelj@thphy.uni-duesseldorf.de

oscillations between the two donors. Due to the particular geometry, a tailored phonon environment is formed for the electron which depends non-monotonously on the phonon frequencies. In order to provide accurate quantitative results on the decoherence and dissipation rates, we apply the numerically exact iterative quasi-adiabatic propagator path integral (QUAPI) scheme [8,9]. In particular, we have improved the widely used method by providing a recipe to completely eliminate the Trotter discretization error. This allows to obtain fully convergent exact results by extrapolation to a vanishing Trotter increment [10]. An appealing alternative to extensive numerical studies are approximative calculations which, for instance, rely on the weak coupling between the qubit and the environment. The most familiar Born-Markov or weak-coupling approximation (WCA) [11] yields to simple closed expression for the decoherence and relaxation rates. However, they apply for typical situations when the bath has a smooth frequency distribution [11]. In our case, the environment is particularly shaped by the geometry leading to a non-monotonous bath spectral density. Hence, it is not a priori clear whether the widely used WCA is appropriate and a careful check is desirable. By comparing the exact numerical QUAPI results with the approximate WCA results below, we will show that for realistic parameters, the WCA typically yields the correct order of magnitude for the decoherence and relaxation rates. However, differences are noticeable when a quantitative comparison is made. We furthermore note that the calculated phonon decoherence and relaxation rates comprise a fundamental upper limit for the coherence properties of this architecture which can hardly be overcome.

The presented set-up is related to a double-quantum dot charge qubit realized in a GaAs semiconductor [12], where the geometrical constraints induce charge qubit oscillations with noticeable non-Markovian corrections due to the particularly shaped phonon environment. While piezoelectric phonons dominate in GaAs, we have to consider here the dominating deformation potential electron-phonon coupling since the Si crystal displays inversion symmetry.

2 The model

To study the influence of the phonons on decoherence and dissipation, we assume that the charge qubit is isolated from any leads. It is formed by a pair of donor atoms embedded in a silicon substrate, which share a single excess electron [3,4]. To be specific, we consider the situation of one donor being a phosphorous atom while the second one is an individual donor atom X chosen from the group $X \in \{\mathrm{Bi, As, P, Sb}\}$ [7]. Then, the two logic states $|0\rangle, |1\rangle$ of the charge qubit are defined by the electron residing either at donor 1 or 2, respectively. The total Hamiltonian is given in terms of the standard spin-boson model [11,13]

$$H = H_S + H_B + H_{SB}\,, \tag{1}$$

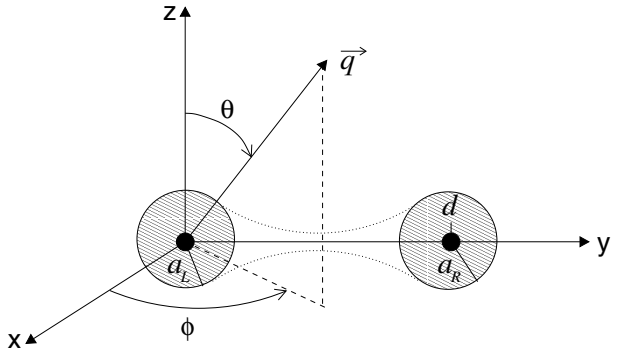

Fig. 1. Sketch of the geometry of a donor-based charge qubit formed two donor atoms at a distance d and the various angles of the phonon propagation.

where H_S is the two-state Hamiltonian for the charge qubit, H_B models the phonon bath and H_{SB} includes the electron-phonon coupling.

2.1 Model for the charge qubit

We represent the Hamiltonian of the charge qubit in the basis of the two localized electronic states denoted as $|L\rangle \equiv |0\rangle$ and $|R\rangle \equiv |1\rangle$, each being the $1s$ orbital of the left/right donor atom, the latter being placed at the origin and at the position $d\mathbf{e}_y$, see Figure 1 for a sketch of the geometry. The localized orbital belonging to the right (left) donor is fully described by the position vector of the electron, i.e., $\mathbf{r}_L = \mathbf{r}$ and $\mathbf{r}_R = \mathbf{r} + d\mathbf{e}_y$, respectively. In addition, we allow for an external constant energy bias ϵ which for instance could be due to a nearby capacitive gate. In terms of the Pauli spin matrices σ_i, the two-state Hamiltonian then reads

$$H_S = \hbar\Delta\sigma_x + \hbar\epsilon\sigma_z. \tag{2}$$

The two lowest lying energy eigenstates $|E^{\pm}\rangle$ are given as an (anti-)symmetric superposition of the localized states $|L\rangle$ and $|R\rangle$ such that $|E^{\pm}\rangle = (|L\rangle \pm |R\rangle)/\sqrt{2}$ with energies $E_{\pm} = \mp\Delta/2$. The tunneling amplitude then follows as $\Delta = E_+ - E_-$ and is a function of the donor distance d.

In order to determine the tunneling amplitude Δ, we have to calculate approximate eigenvalues of the lowest symmetric and antisymmetric energy-eigenstate. In principle, rather highly elaborated methods are available for their calculation, including the anisotropic conduction band dispersion of silicon, the valley orbit interaction and valley interference effects [7,14]. The latter leads to an oscillatory behavior of the tunneling amplitude Δ for increasing the donor distance d. Noticeably, the oscillations are weak if the two donors are placed in the [100]-plane of the Si host [7]. However, we aim for a detailed and quantitative understanding of the electron-phonon decoherence mechanism and thus resort to the simplest straightforward procedure to determine the tunneling amplitude which is the well established linear combination of atomic orbitals (LCAO) [3,15]. This tight-binding method is very

successful for determining the molecular orbitals for the H_2^+-molecule but can easily be generalized to our model by introducing an effective Bohr radius [16]. When we neglect the conduction-band anisotropy, we can assume that the localized states $|\xi\rangle$ ($\xi = L, R$) are represented by the $1s$ orbital of each donor. They read

$$|\xi\rangle = \sqrt{\frac{1}{\pi a_\xi^3}} e^{-r_\xi/a_\xi} \tag{3}$$

where a_ξ is the effective Bohr-radius of the donor ξ [16] and $r_\xi = |\mathbf{r}_\xi|$. In the following, the left donor is assumed to be the phosphorous atom, whereas the right donor is taken from the group-V donors {Bi, As, P, Sb}. Hence, we introduce the ratio p such that $a_R = pa_L$.

To calculate the energy levels an ansatz for the wave function for the (anti-)symmetric ($\mp$) part is made and the overlap between the two wave functions is calculated, yielding the energies for the (anti-)symmetric state. If energies are scaled in atomic units, they read [15]

$$E_\pm = E_1^{(\pm)}(d) + E_2^{(\pm)}(d)\,. \tag{4}$$

Here, $E_1^{(\pm)}(d)$ is the kinetic energy and $E_2^{(\pm)}(d)$ is the potential energy, both being functions of the (dimensionless) donor distance d. They read

$$\begin{aligned} E_1^{(\pm)}(d) &= \frac{1 \pm e^{-d}(1 + d - d^2/3)}{1 \pm e^{-d}(1 + d + d^2/3)} \\ E_2^{(\pm)}(d) &= -2\frac{1 \pm 2\,e^{-d}(1+d) + (1/d) - (1/d+1)\,e^{-2d}}{1 \pm e^{-d}(1 + d + d^2/3)}\,. \end{aligned} \tag{5}$$

Due to the fixed positions of the donors, there is no need to minimize the energy with respect to the donor distance, in contrast to analogous calculations for the H_2^+-molecule. According to the LCAO calculations typical tunneling amplitudes for a distance of $d = 7.06$ nm (which corresponds to a separation of the two dopants by $n = 13$ lattice sites) follow as $\Delta \approx 16$ meV. This is qualitatively consistent with the results obtained from a more refined approach taking into account interference effects in the Si band structure [7].

2.2 Coupling to linear acoustic phonons

The phonon bath is due to the silicon host crystal and is modeled as usual in terms of the bosonic operators $b_\mathbf{q}$ as

$$H_B = \hbar \sum_\mathbf{q} \omega_\mathbf{q} b_\mathbf{q}^\dagger b_\mathbf{q}\,, \tag{6}$$

with the phonon dispersion relation $\omega_\mathbf{q}$. The electron-phonon interaction reads [17,18]

$$H_{SB} = \hbar \sum_\mathbf{q} (\alpha_\mathbf{q}^L N_L + \alpha_\mathbf{q}^R N_R)(b_\mathbf{q}^\dagger + b_{-\mathbf{q}})\,. \tag{7}$$

Here, $N_\xi = 0, 1$ is the number of the excess electrons on the donor ξ, respectively, and $\alpha_\mathbf{q}^\xi = \lambda_\mathbf{q} e^{-i\mathbf{q}\cdot\mathbf{r}_\xi} F_\xi(\mathbf{q})$. The coupling constant $\lambda_\mathbf{q}$ depending on the wave vector $\mathbf{q}$ is specified below. Note that the phonons can propagate in all three dimensions, and the electron-phonon coupling is not isotropic in general [19]. To take care of the charge distribution in each donor we define a form factor according to

$$F_\xi(\mathbf{q}) = \int d^3r\, n_\xi(\mathbf{r}) e^{-i\mathbf{q}\cdot\mathbf{r}}\,, \tag{8}$$

where $n_\xi(\mathbf{r})$ is the charge density of the donor ξ. The coupling Hamiltonian is rewritten in the form [18]

$$H_{SB} = \frac{\hbar}{2}\sigma_z \sum_\mathbf{q} g_\mathbf{q}(b_\mathbf{q}^\dagger + b_{-\mathbf{q}})\,, \tag{9}$$

with $g_\mathbf{q} = [\lambda_\mathbf{q}(F_L(\mathbf{q}) - F_R(\mathbf{q}))]$. The charge density distribution then follows directly from equation (3) as $n_\xi(\mathbf{r}) = |\langle\mathbf{r}|\xi\rangle|^2$, which leads to the form factors $F_L(\mathbf{q}) = f_L(\mathbf{q})$ and $F_R(\mathbf{q}) = f_R(\mathbf{q}) e^{-i\mathbf{q}\cdot d\mathbf{e}_y}$ with $f_\xi(\mathbf{q}) = 16/[4 + (qa_\xi)^2]^2$.

In this work we focus on linear acoustic phonons with linear dispersion relation $\omega_\mathbf{q} = s|\mathbf{q}|$, s being the sound velocity for silicon ($s \approx 9 \times 10^3$ m/s) [20]. Since the silicon crystal has an inversion center there is no piezoelectric coupling between electrons and phonons, wherefore the dominating coupling is due to the deformation potential. Thus, the coupling constant reads

$$\lambda_\mathbf{q} = \frac{D}{\hbar} q \sqrt{\frac{\hbar}{2\rho_m V \omega_\mathbf{q}}}, \tag{10}$$

where D is the deformation constant for silicon ($D \approx 8.6$ eV, see Ref. [21]), ρ_m is the mass density of silicon ($\rho_m \approx 2.33 \times 10^3\,\mathrm{kg\,m^{-3}}$, see Ref. [20]) and V is the volume of the unit cell.

All the properties of the phonon bath can be captured in the spectral density defined as

$$G(\omega) = \sum_\mathbf{q} |g_\mathbf{q}|^2 \delta(\omega - \omega_\mathbf{q})\,. \tag{11}$$

Using equation (10) and the definition of the form factors and taking into account the geometry, the sum over $\mathbf{q}$ can be transformed into a continuous integral which can readily be carried out. One then obtains the spectral density

$$\begin{aligned} G(\omega) = &\frac{64D^2}{\pi^2\rho_m\hbar s^5}\omega^3 \left[\left(4 + \left(\frac{\omega}{s}a_L\right)^2\right)^{-4}\right. \\ &+ \left(4 + \left(\frac{\omega}{s}pa_L\right)^2\right)^{-4} - 2\left(4 + \left(\frac{\omega}{s}a_L\right)^2\right)^{-2} \\ &\left.\times \left(4 + \left(\frac{\omega}{s}pa_L\right)^2\right)^{-2} j_0\left(\frac{\omega}{s}d\right)\right]. \end{aligned} \tag{12}$$

where j_0 is the spherical Bessel function. The spectral density is sketched in the inset of Figure 2. The low-frequency behavior is superohmic according to $G(\omega \to 0) \propto \omega^3$, while in the high-frequency limit, it decays algebraically as

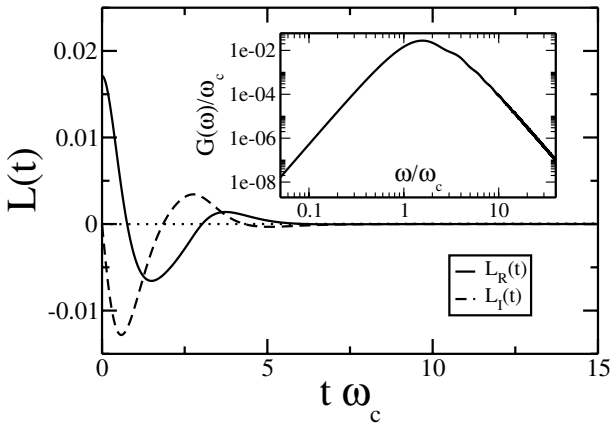

Fig. 2. The bath autocorrelation function (response function) $L(t) = L_R(t) + iL_I(t)$ for the spectral density $G(\omega)$ (inset) of the phonon bath for the case of two P donors in a Si host ($p = 1$, deformation potential phonons), with $s = 9 \times 10^3$ m/s, an effective Bohr radius of $a_P = 1.22$ nm, and inter-donor distance $d = 10.32$ nm. The temperature is $T = 50$ mK.

$G(\omega \to \infty) \propto \omega^{-5}$. The crossover between these two limits occurs on a frequency scale $\omega_c = s/a_P \equiv \tau_c^{-1}$, where a_P is the radius of the phosphorus donor ($a_P = 1.22$ nm, see Ref. [16]), yielding $\omega_c = 2.46$ THz, which corresponds to an energy of 10.17 meV. As we will see below, typical tunneling amplitudes Δ are comparable to this energy scale. Thus, the frequency distribution of the bath is no longer monotonous in the range of the relevant system energies. As common approximative analytical treatments [3,11] of phonon-induced decoherence typically involve a smooth frequency distribution, it is not a priori clear whether their results are applicable to this situation. Moreover, the used Born-Markovian approximation which neglects bath-induced correlations might not describe properly the dynamics. This can be seen from the autocorrelation function [11] of the bath, i.e.,

$$L(t) = L_R(t) + iL_I(t) = \frac{1}{\pi}\int_0^\infty d\omega G(\omega)\left[\coth\frac{\hbar\omega\beta}{2}\cos\omega t - i\sin\omega t\right], \quad (13)$$

which is shown in Figure 2. The typical width of the correlation function is comparable to the time scale $\Delta^{-1} \approx \omega_c^{-1}$ of the system dynamics. The Born-Markov approximation corresponds to replacing the strongly peaked real part $L_R(t)$ by a δ-function with the corresponding weight while the imaginary part $L_I(t)$ is often neglected. However, since the geometry tailors a specific structured phonon environment for the charge qubit, it is not clear from the very beginning that the Markovian assumption is valid. It is the main purpose of this work to investigate this issue and compare exact real-time path integral simulations with approximate weak-coupling (Born-Markov) results.

3 The improved QUAPI scheme

The dynamics of the charge qubit is described in terms of the time evolution of the reduced density matrix $\rho(t)$ which is obtained after tracing out the bath degrees of freedom, hence

$$\rho(t) = \mathrm{tr}_B K(t,0)W(0)K^{-1}(t,0)\,,$$
$$K(t,0) = \mathcal{T}\exp\left\{-\frac{i}{\hbar}\int_0^t dt' H\right\}. \quad (14)$$

$K(t,0)$ denotes the propagator of the full system plus bath, $\mathcal{T}$ is the time ordering operator and H is the Hamiltonian, equation (1). The full density operator $W(0)$ at initial time $t = 0$ is as usual assumed factorizing according to $W(0) \propto \rho(0)\exp[-H_B/(k_BT)]$, where k_B is the Boltzmann constant and T is the bath temperature [11]. In this work the qubit dynamics always evolves from the initial state $\rho(0) = |L\rangle\langle L|$.

In order to investigate the dynamics of the system, we use the quasi-adiabatic propagator path integral (QUAPI) scheme [8] being a numerically exact iteration scheme which has been successfully adopted to many problems of open quantum systems [9,12]. For details of the iterative scheme we refer to previous works [8,9] and do not reiterate the scheme here again. However, we have improved the method at one important step and we will describe this in greater detail next.

The algorithm is based on a symmetric Trotter splitting of the short-time propagator $K(t_{k+1}, t_k)$ of the full system into a part depending on H_S and $H_B + H_{SB}$ describing the time evolution on a time slice Δt. This is exact in the limit $\Delta t \to 0$ but introduces a finite Trotter error to the propagation which has to be eliminated by choosing Δt small enough that convergence has been achieved. On the other side, the bath-induced correlations being nonlocal in time are included in the numerical scheme over a finite memory time $\tau_{mem} = K\Delta t$ which roughly corresponds to the time range over which the bath autocorrelation function $L(t)$ given in equation (13) is significantly different from zero. Note that for any finite temperature $L(t)$ decays exponentially at long times [11] justifying this approach. To obtain convergence with respect to the memory time, K has to be increased until converged results have been found. However, the numerical effort grows exponentially with the memory length K and for the present two-level system, the memory length is restricted to typical values of $K = 12$ on a standard processor with 2 GB RAM for practical reasons.

Thus, the two strategies to achieve convergence are countercurrent. To solve this, the principal of least dependence has been invoked [9] to find an optimal time increment in between the two limits. However, here we show that the algorithm can be improved by applying a different strategy.

We first choose some small enough time increment Δt. Then, one has to increase the memory time τ_{mem} by increasing K until convergence has been achieved. Typical results of this memory convergence check are shown in

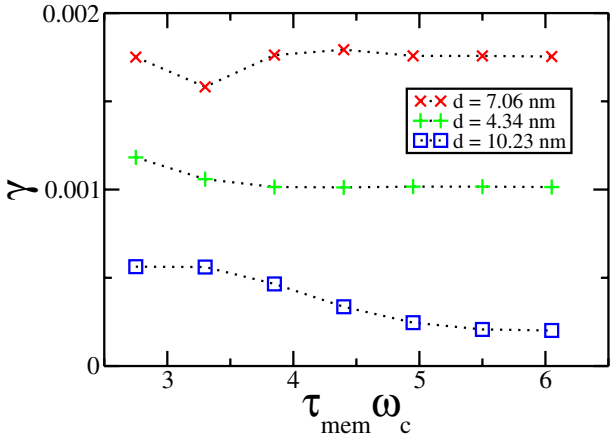

Fig. 3. (Color online) Check of convergence with respect to the memory time $\tau_{mem} = K\Delta t$ for the decoherence rate γ (symmetric qubit $\epsilon = 0$) and for the donor distances $d = 4.34\,\mathrm{nm}$, $d = 7.06\,\mathrm{nm}$ and $d = 10.32\,\mathrm{nm}$ and the corresponding tunnel matrix elements obtained from the LCAO. The Trotter time increment is fixed to $\Delta t = 0.55\omega_c$.

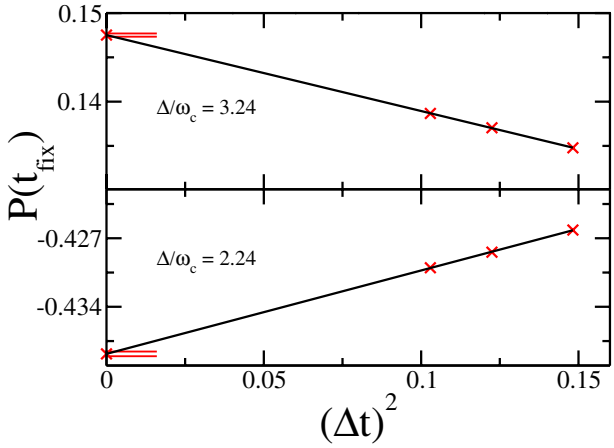

Fig. 4. (Color online) Example of the Trotter convergence for the the population difference of the qubit, $P(t_{fix})$, from which the quantities of interest are extracted. In the lower sketch the tunnel amplitude was chosen as $\Delta/\omega_c = 2.24$ and $t_{fix} = 34.1\omega_c$, and in the upper sketch $\Delta/\omega_c = 3.24$ and $t_{fix} = 18.2\omega_c$. The memory-time is fixed to $\tau_{mem} = 3.85/\omega_c$ and three values of $K = 10, 11, 12$ have been chosen. At $\tau_{mem}^2/K^2 \to 0$ the value $P(t_{fix})$ is shown as a result of the extrapolation $\Delta t \to 0$, with the error of the linear regression (horizontal bars).

Figure 3. Shown is the decoherence rate γ for increasing memory time for different donor distances ($p = 1$) for the symmetric qubit $\epsilon = 0$. Note that the decay rate has been obtained by fitting the results for the population difference $P(t) = \langle\sigma_z\rangle_t$ to an exponentially decaying cosine. The remaining error is the Trotter error. However, following reference [10], for any Hermitian observable, this symmetric Trotter error vanishes quadratically in the limit $\Delta t \to 0$. This opens the possibility to extrapolate the results to $\Delta t \to 0$, thereby completely eliminating the Trotter error. This is done by decreasing Δt from the initial value and then by finding the extrapolated exact result (of course, convergence has to be verified again for the smaller values of Δt). Typical results of this extrapolation procedure are shown in Figure 4, indicating that the numerical values follow a line for decreasing step sizes. Note that we consider $P(t_{fix})$ at an arbitrary time $t_{fix} = 34.1\omega_c$ in this example. Indeed, we find the predicted behavior for the Trotter error to vanish and perform a linear regression to $\Delta t \to 0$, also shown in Figure 4. The y-axis intersection gives the numerical exact value for the observable of interest, in this case afflicted with a tiny error bar coming from the linear regression. In general, the convergence properties of an observable strongly depend on the involved parameters, similar to path-integral quantum Monte-Carlo simulations [22]. Different observables show different behaviors with decreasing Trotter step size Δt, as for instance the particle density in contrast to the energy of the system in reference [22].

4 The dynamics of the charge qubit

Equipped with the numerically exact improved QUAPI scheme, we can now study the dynamics of the charge qubit in detail. To extract the decoherence rate γ, the relaxation rate γ_r, the equilibrium population difference P_∞ and the oscillation frequency Ω, we fit a combination of exponentially decaying cosine and sine functions [11] to the numerically exact data, from which the Trotter error has been eliminated. We can then investigate the dependence of the above quantities on the experimentally relevant parameters. We emphasize again that realistic assumptions on the geometry of the system enter the spectral density equation (13) and thus allow to calculate quantitative realistic results.

One of the major goals of this work is to verify the Born-Markov (weak-coupling) approximation, since the later results in very simple and compact formulas for parameters governing the dynamics. Hence, we compare the exact QUAPI results with results obtained within a WCA which are known as [11]

$$\gamma = \frac{\gamma_r}{2} + \frac{2\pi\epsilon^2}{\Delta_b^2}\, S(0)\,, \tag{15}$$

$$\gamma_r = \frac{\pi\Delta_{\mathrm{eff}}^2}{2\Delta_b^2}\, S(\Delta_b)\,, \tag{16}$$

$$\Omega^2 = 4\Delta_{\mathrm{eff}}^2[1 - 2\,\mathrm{Re}\,u(2i\Delta_b)] + 4\epsilon^2\,, \tag{17}$$

$$P_\infty = -\frac{\epsilon}{\Delta_b}\tanh\left(\frac{\hbar\Delta_b\beta}{2}\right)\,. \tag{18}$$

The spectral function $S(\omega)$, related to the phonon spectral density, equation (13), via $S(\omega) = G(\omega)\coth(\hbar\omega/(2k_BT))$, represents emission and absorption of a single phonon and $\Delta_b = 2\sqrt{\Delta_{\mathrm{eff}}^2 + \epsilon^2}$ is twice the effective qubit frequency. Δ_{eff} is the effective tunnel matrix element at $T = 0$ [11], which includes the renormalization by a Franck-Condon factor stemming from the high-frequency modes of the reservoir [11]. For our case, one easily finds that $\Delta_{\mathrm{eff}} \approx \Delta$

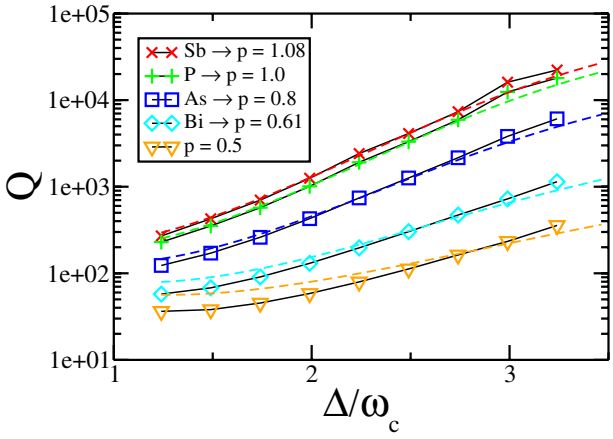

Fig. 5. (Color online) Quality factor as a function of the tunneling amplitude Δ for different donor combinations and a small donor distance $d = 4.34$ nm. The symbols depict the exact QUAPI results while the dashed lines mark the results of the WCA. Temperature is fixed at $T = 50$ mK.

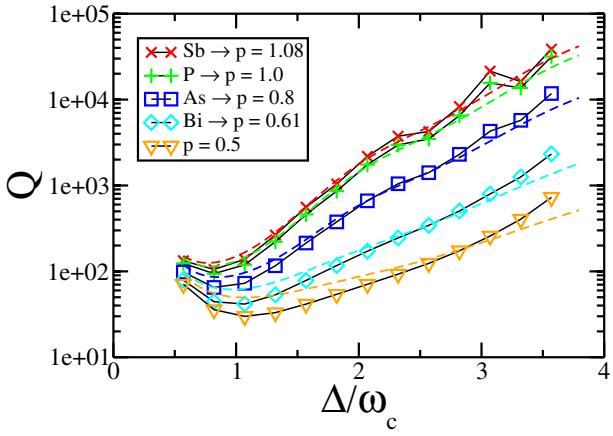

Fig. 6. (Color online) Same as Figure 5, but for an intermediate donor distance $d = 7.06$ nm.

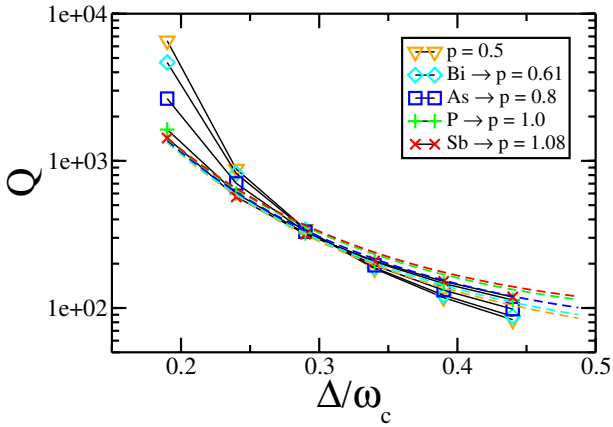

Fig. 7. (Color online) Same as Figure 5, but for a large donor distance $d = 10.32$ nm.

with a deviation of less than 1%. The function $u(z)$ is defined in terms of the frequency integral

$$u(z) = \frac{1}{2}\int_0^\infty d\omega \, \frac{G(\omega)}{\omega^2 + z^2}\left(\coth\left(\frac{\hbar\omega}{2k_BT}\right) - 1\right). \quad (19)$$

4.1 Coherent charge oscillations for the symmetric qubit $\epsilon = 0$

For the symmetric qubit with zero bias (i.e., only decoherence, no dissipation), we have calculated the time evolution of $P(t)$ and have observed coherent charge oscillations. In order to quantify them, we define the quality factor $Q = \Omega/(\pi\gamma)$ where the frequency Ω and the decoherence rate γ have been been obtained from the fit as described above. We have performed extensive simulations for three different donor distances d for various combinations of donor atom species and show the results as a function of the tunneling amplitude Δ in Figures 5–7, each for a fixed donor distance d. A variation of Δ for a fixed donor distance can, for instance, be achieved by a small additional gate voltage which slightly distorts the $1s$ orbitals leading to an increased overlap of the wave functions.

For the smallest donor distance $d = 4.34$ nm, we observe in Figure 5 that Q increases monotonously for increasing Δ. Thereby, the results for Q vary over two orders of magnitude for the different donor species at large Δ. Moreover, the combination of two P donors or of one P and one (very similar) Sb donor displays the best decoherence properties. The dashed lines in Figure 5 display the results of the WCA given in equations (15) and (17). A reasonable agreement is found in this case.

For intermediate donor distance $d = 7.06$ nm, see Figure 6, Q first decreases but then increases again with increasing Δ. This can be understood by the fact that d determines the shape of the spectral density and, in particular, the location of the frequency of the cross-over, relative to the qubit frequency Δ. For the overall performance, the similar observation as for the smaller distance (see above) apply. Also in this case, the WCA seems to be appropriate although small deviations for all Δ can be observed which can be attributed to small non-Markovian corrections stemming from the specifically tailored phonon environment.

In the case of large donor distance $d = 10.32$ nm, see Figure 7 the differences between the various donor species almost vanish and are only noticeable at small Δ. Also the WCA agrees well at large Δ and also yields the correct order of magnitude for small Δ although differences become noticeable in this regime. Note that in this case, Q decreases for increasing Δ, in contrast to the case of small and intermediate distances.

Noticeably, we find that the Q-factor is independent of temperature for all relevant parameter combinations (not shown here). This is due to the fact that realistic temperatures correspond to frequencies of $T = 6.5 \times 10^9$ Hz and hence all system frequencies are much larger. This behavior is in contrast to what we have recently reported in GaAs DQD systems [12].

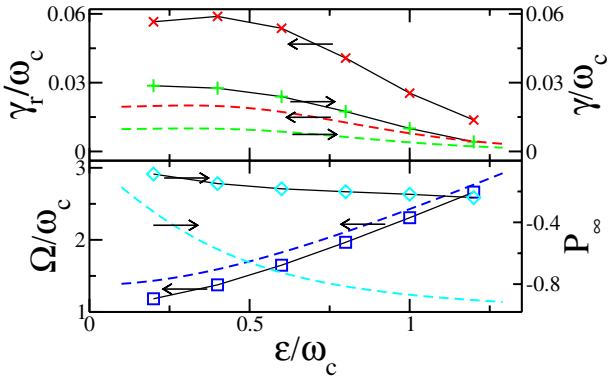

Fig. 8. (Color online) Upper panel: relaxation (γ_r) and decoherence (γ) rate for increasing bias ϵ. Symbols are the exact QUAPI results while the dashed lines are the corresponding WCA results. Lower panel: oscillation frequency Ω and asymptotic value P_∞. The remaining parameters are $d = 7.06$ nm, $\Delta = 0.57\omega_c$, and $T = 50$ mK.

Note that the oscillatory behavior of Δ for increasing d [7] is not included in this simple LCAO approximation. However, when considering the Q-factor in Figures 5–7, the oscillatory behavior of Δ for growing donor distances d does not affect Q substantially. This can be rationalized by considering the weak-coupling results equations (15–17) for $\epsilon = 0$. Then, it becomes clear that the only part where $\Delta(d)$ appears is in the high-frequency part of $G(\omega)$ (assuming low temperature such the the coth approaches one and being interested in $\Delta \approx \omega_c$). The prefactors, which in principle contain $\Delta(d)$, drop out when the ratio is calculated.

4.2 Dynamics of the biased charge qubit $\epsilon \neq 0$

When a finite bias $\epsilon \neq 0$ is present, in addition to decoherence also relaxation occurs to a non-zero asymptotic value $P_\infty \neq 0$. The corresponding decoherence and relaxation rates are also influenced by the presence of a bias in the sense that the effective qubit frequency Δ_b grows with increasing ϵ. Then, the behavior of the environmental frequency distribution is essential: if it grows with increasing frequency, decoherence and dissipation will become more effective and if it decreases the environmental effects will diminish. This is what we observe from the results shown in Figure 8. For comparison, we also show the corresponding WCA results, which yield the qualitatively correct behavior while differences in the quantitative results occur.

5 Conclusion

To summarize, we have investigated the phonon-induced decoherence and dissipation in donor-based charge qubits formed by a pair of donor atoms placed in a Si crystal host. The donor pair is formed by one P donor and one donor of the group Bi, As, P, Sb. We have employed the numerically exact quasi-adiabatic path-integral propagator in its iterative version. The major achievements of our work is twofold: (i) we have first improved the QUAPI scheme in the sense that the Trotter discretization error can now be completely eliminated by extrapolating the results to vanishing Trotter increment, as it is known that the error vanishes quadratically; (ii) beyond these methodical aspects, we have obtained numerically exact results for the real-time dynamics of charge qubits under the influence of acoustic deformation potential phonons. Realistic assumptions on the tunneling amplitude enter via LCAO calculations of the wave functions and the qubit energies in our model. Moreover, we have included the particular phonon environment tailored by the particular geometry of the set-up via geometrical form factors and materials characteristics. No fitting parameters of any sort were utilized.

In the absence of a static bias we have investigated the Q-factor of the charge oscillations as a function of the donor distance and as well as a function of the tunneling amplitude. We have compared our results with those obtained from a WCA within an analytical approach in terms of real-time path-integrals and found that only small non-Markovian corrections appear. This can be attributed to the dominating super-Ohmic properties of the phonon environment at small frequencies. Furthermore we have investigated the dynamics in the case of a static bias and have found that the qualitative behavior of the decoherence and damping rates follows the form of the environmental frequency distribution. Non-Markovian corrections are also found in this case.

At present, no experimental realizations of this setup is yet reported. Nevertheless, we emphasize that our results on the decoherence and dissipation induced by the electron-phonon coupling represent a fundamental upper limit to the coherence of such donor based charge qubits which can hardly be negotiated due to its intrinsic nature. This has to be seen in view of the DiVincenzo criteria [23] and also for the future realization of quantum information processes. However, the dominating source of decoherence in this kind of qubit realization has to be investigated in realistic devices.

This work was supported by the ESF network INSTANS, the DFG-SFB Transregio 12, and the DFG Priority Program 1243.

References

1. For a review, see the Focus Issue on Solid State Quantum Information, edited by R. Fazio, New J. Phys. **7** (2005)
2. B.E. Kane, Nature (London) **393**, 133 (1998)
3. S.D. Barrett, G.J. Milburn, Phys. Rev. B **68**, 155307 (2003)
4. L.C.L. Hollenberg, A.S. Dzurak, C. Wellard, A.R. Hamilton, D.J. Reilly, G.J. Milburn, R.G. Clark, Phys. Rev. B **69**, 113301 (2004)
5. D.R. McCamey, H. Huebl, M.S. Brandt, W.D. Hutchison, J.C. McCallum, R.G. Clark, A.R. Hamilton, preprint `arXiv:cond-mat/0605516`
6. M. Thorwart, P. Hänggi, Phys. Rev. A **65**, 012309 (2002)

7. B. Koiller, X. Hu, S. Das Sarma, Phys. Rev. B **73**, 045319 (2006); X. Hu, B. Koiller, S. Das Sarma, Phys. Rev. B **71**, 235332 (2005)
8. D.E. Makarov, N. Makri, Chem. Phys. Lett. **221**, 482 (1994); N. Makri, D.E. Makarov, J. Chem. Phys. **102**, 4600 (1995); N. Makri, D.E. Makarov, J. Chem. Phys. **102**, 4611 (1995); N. Makri, J. Math. Phys. **36**, 2430 (1995)
9. M. Thorwart, P. Reimann, P. Jung, RF. Fox, Chem. Phys. **235**, 61 (1998); M. Thorwart, P. Reimann, P. Hänggi, Phys. Rev. E **62**, 5808 (2000); M. Thorwart, E. Paladino, M. Grifoni, Chem. Phys. **296**, 333 (2004)
10. R.M. Fye, Phys. Rev. B **33**, 6271 (1986)
11. U. Weiss, *Quantum Dissipative Systems,* 2nd edn. (World Scientific, Singapore, 1999)
12. M. Thorwart, J. Eckel, E.R. Mucciolo, Phys. Rev. B **72**, 235320 (2005)
13. A.J. Leggett, S. Chakravarty, A.T. Dorsey, M.P.A. Fisher, A. Garg, W. Zwerger, Rev. Mod. Phys. **59**, 1 (1987)
14. C.J. Wellard, L.C.L. Hollenberg, Phys. Rev. B **72**, 085202 (2005)
15. J.C. Slater, *Quantum Theory of Molecules and Solids,* Vol. 1 (McGraw-Hill, New York, 1963)
16. T.H. Ning, C.T. Sah, Phys. Rev. B **4**, 3468 (1971)
17. G.D. Mahan, *Many-particle physics* (Plenum Press, New York, 1981)
18. T. Brandes, B. Kramer, Phys. Rev. Lett. **83**, 3021 (1999); T. Brandes, T. Vorrath, Phys. Rev. B **66**, 075341 (2002)
19. S. Vorojtsov, E.R. Mucciolo, H.U. Baranger, Phys. Rev. B **71**, 205322 (2005)
20. MSM archive at `http://www.ioffe.rssi.ru/SVA/NSM/`
21. M. Friedel, M.S. Hybertsen, M. Schlüter, Phys. Rev. B **39**, 7974 (1989)
22. S. Weiss, R. Egger, Phys. Rev. B **72**, 245301 (2005)
23. D.P. DiVincenzo, Fortschr. Phys. **48**, 771 (2000)